Experimental Mechanics (2019) 59:843–857
https://doi.org/10.1007/s11340-019-00498-z

Mechanical Properties of Printed Epoxy-Carbon Fiber Composites

H.A. Pierson[1] · E. Celik[2] · A. Abbott[3] · H. De Jarnette[4] · L. Sierra Gutierrez[5] · K. Johnson[3] · H. Koerner[3] · J.W. Baur[3]

Received: 1 November 2018 / Accepted: 1 March 2019 / Published online: 28 March 2019

Abstract

Despite the promise of additive manufacturing (AM) to bring unprecedented agility and design freedom to manufactured components, structural applications remain largely out of reach due to material restrictions – notably the lack of a mature AM process for reinforced thermoset composites. AM is also hindered by process-induced defects such as porosity and unfavorable microstructure. This research shows that a direct write AM process for epoxy / chopped carbon fiber composites can simultaneously achieve a high degree of fiber alignment and low degree of porosity, obtaining 90% of the theoretical tensile modulus and 66% of the theoretical tensile strength for a fully aligned composite. These values exceed those of compression molded properties for the same material. Transverse properties of AM samples were roughly half of the longitudinal properties but showed no statistically significant difference from the matrix material, suggesting that the process may not adversely affect microstructure. The addition of only 5.5 vol% carbon fiber more than doubled the strength and stiffness of the neat epoxy, and more than tripled the properties of ABS thermoplastic while achieving a higher glass transition temperature. Flexural properties show similar trends. SEM and CT imaging shows that fiber orientation is largely maintained in the print direction and cross-section micrographs show there is sufficient local material flow during deposition to achieve low porosity.

Keywords Additive manufacturing · 3D printing · Composites · Carbon fiber · Direct write · Thermoset

Introduction

Additive manufacturing (AM) is rapidly maturing from a prototyping tool into a mainstream manufacturing process. This transition is driven by several key advantages: Cost is mostly independent of geometry, reducing design constraints associated with other manufacturing processes [1]. This enables topology-optimized designs [2, 3], consolidation of assemblies into a single component [4–6], internal geometry, and thin-walled structures. No tooling is required, resulting in short lead times and potential for economical low-quantity production [7]. Compactness and geometric flexibility enable distributed production models [8] and remote fabrication capabilities for space exploration [9, 10] or in-theater manufacturing for the military [11]. AM can also make other manufacturing processes more agile by rapidly producing layup molds, casting patterns, welding jigs, and other tooling [12].

Despite these advantages, key challenges hinder the application of AM to manufactured components and tooling. Current commercial AM technology restricts material choice, with a notable void in the space of high specific strength, specific stiffness, service temperature, and environmental survivability typically occupied by thermoset composites. AM process also tend to result in inferior properties relative to traditional manufacturing processes. Within the realm of polymer AM, fused filament fabrication (FFF) processes impart porosity [13], and both inter-layer and inter-road bonds are generally weaker than the base material [14, 15]. Both filament- and powder-based processes subject materials to repeated heat-cool cycles that can adversely affect geometric precision and inter-layer bonding. Repeated local phase changes and complex thermal histories combine with complex

✉ J. W. Baur
jeffery.baur@us.af.mil

[1] Department of Industrial Engineering, University of Arkansas, 4172 Bell Engineering Center, Fayetteville, AR 72701, USA

[2] Department of Aerospace and Mechanical Engineering, University of Miami, 1251 Memorial Dr, Coral Gables, FL 33146, USA

[3] Materials and Manufacturing Directorate, Air Force Research Laboratory, Wright-Patterson Air Force Base, OH 45324, USA

[4] Department of Mechanical Engineering, Louisiana Tech University, 305 Wisteria St., Ruston, LA 71272, USA

[5] Department of Mechanical Engineering, University of Texas at El Paso, 1981 Hawthorne St., El Paso, TX 79968, USA

geometries to result in complicated material-process-property relationships that make predicting and controlling as-built properties difficult.

Typical AM thermoplastic polymer materials include Acrylonitrile Butadiene Styrene (ABS), Polylactic Acid (PLA), Nylon, and Polyethylene Terephthalate Glycol (PETG). Their properties are well documented in literature [16–19]. To enhance the mechanical properties of these thermoplastic polymers, high-strength fibers have been added [20–25]. In these studies, tensile and bending properties were characterized for glass, carbon, and Kevlar fiber reinforced specimens fabricated via FFF. Although this improves mechanical properties, issues with low service temperature, unavoidable porosity, suboptimal bonding between roads/layers, and difficulty controlling printing parameters (i.e., printing pattern in continuous fiber deposition) remain significant drawbacks.

A recently developed direct write method avoids many of the drawbacks of fiber reinforced thermoplastic printing [26]. Direct write is a fluid deposition process which relies on the fluid's yield stress to form self-supporting structures. The process involves preparing printable inks by adjusting the fluid viscosity and yield strength using rheological modifiers such as nanoclay. Since material melting is not required for printing, thermosetting polymers are printable with this method. The entire printed structure is printed at room-temperature and cured in a secondary process which simplifies the process and significantly reduces the dependence of the mechanical properties on thermal printing history and spatial heating path. The direct write method has been applied to the fabrication of silicon carbide, chopped carbon fiber, and nanoclay reinforced thermosets [26, 27]. Recently, the method was further enhanced for printing of helically oriented fibers to achieve improved damage performance [28].

Although these previous studies have shed light upon AM of fiber reinforced composites, the effects of process parameters on the mechanical performance are not yet fully understood. This study explored process parameters including fiber length, fiber loading, and fiber orientation on the mechanical performance of additively manufactured thermoset composites. Unlike the previous studies, mechanical properties of additively manufactured composites were compared to those fabricated via compression molding. In addition, some previous studies reported that carbon fiber addition lowered the tensile mechanical properties [26, 29] of thermosetting composites; however, this research demonstrated increased tensile strength and stiffness as a function of the fiber content. This study will therefore complement the previously published studies and reduce the knowledge gap on AM of composites with high strength and high temperature resistance properties.

Experimental Procedures

Ink Formulation & Processing

The inks tested in this work consist of epoxy resin, curing agent, nanoclay, and chopped carbon fiber. Since AM can be a slow process in which deposition can take hours or even days, a latent curing agent is required to extend the working time of the ink. Nanoclay is included as a rheology modifier, imparting pseudoplasticity and a yield stress to the otherwise Newtonian resin so that the ink may form self-supporting structures.

The epoxy system is EPON Resin 826 from Hexion, Inc. mixed with 5 parts per hundred (pph) by weight ionic liquid imidazole curing agent from Sigma-Aldrich (1- Ethyl-3-methylimidazolium dicyanamide). This system exhibits negligible curing at room temperature and has a pot life on the order of weeks. Flowability can be impeded by epoxy crystallization over the course of days; however, this can be reversed by soaking at 40 °C for 1 h. The clay is Garamite-7305 from BYK additives, which is a mixture of sepiolite and montmorillonite clays. The carbon fiber is 5 μm diameter AS type from Hexcel with BR102 sizing in the form of 6 mm chopped tape.

Ink mixing proceeded as follows: 1) Mix epoxy, curing agent, and nanoclay in a high-shear planetary mixer[1] at 3600 RPM for 5 min. 2) Mix under vacuum in a high-shear planetary mixer[2] at 2000 RPM for 3 min. At this point the mixture is referred to as base ink. 3) Add chopped fiber tape and mix under vacuum in a high-shear planetary mixer at 2000 RPM until the fibers are dispersed. The criterion for dispersion was defined as the ability to extrude 3 cc of the material through a 580 μm tapered orifice at 3.75×10^{-3} cc/s with no flow blockages. High-shear mixing with the fiber generates significant heat, so the final mixing step was limited to 3-min increments with 3-min cooling periods in ambient air.

The goal of the base ink processing procedure is to disperse the clay into the epoxy and remove entrapped air. A portion of the Garamite clay consists of montmorillonite, a nanoscale layered silicate. The exfoliation state of the layers is sensitive to shear forces during the mixing process which impacts ink viscosity and yield stress. High-shear mixing has been used to intercalate and eventually exfoliate these structures [30]. Full exfoliation of the clay is beneficial because, for a given clay loading, yield stress is maximized. Without sufficient mixing, agglomerates (tactoids) do not sufficiently exfoliate and will manifest as a mix-time dependent rheology. In the base ink mixing procedure, step 1 is intended to disperse clay into epoxy with high-shear forces while step 2 is intended primarily as a degassing operation. While the exfoliation state of the

[1] SpeedMixer model DAC 150 FVZ, FlackTek Inc., https://speedmixer.com
[2] THINKY model ARV-310, THINKY Corp., https://thinkyusa.com

montmorillonite portion of the clay was not measured directly, the rheology of the mixed base ink was similar to that of probe sonicated base ink.

Experimental Rational & Design

As fiber loading increases, more mixing time is required to achieve dispersion; however, the interactions between carbon fiber particles during mixing decrease mean fiber length. This leads to a processing window in the fiber length–loading space in which fibers are dispersed and printing is feasible (Fig. 1). The boundary of the feasible region is defined by the minimum mixing time to achieve dispersion and represents the greatest possible mean fiber length for a given loading for this system. Given that longer fibers afford higher stiffness and strength up to a critical value, and do not degrade these properties beyond that critical value [31–33], inks near the upper boundary of the processing window are mechanically superior. This is the primary motivation for studying the effect of mixing time on fiber length. However, fiber loading also improves strength and stiffness, leading to a tradeoff between fiber length and loading. Four inks from the upper boundary of the processing window were selected to explore this tradeoff (Table 1).

AM processes in general are known to produce anisotropic mechanical properties, and this is compounded by the tendency for the fibers to align parallel to the print direction [21, 34, 35]. In the first phase of the experiment, AM mechanical properties for all inks were measured parallel to the print direction since this is the orientation in which fiber length should have the largest effect. Once the best ink in the longitudinal (0°) direction was identified, it was also printed in a transverse (90°) direction to evaluate material properties in the weakest direction (Fig. 2). This ink was also printed in a 2-layer crosshatch pattern (±45°) and a 4-layer quasi-isotropic pattern (0°, 45°, −45°, 90°) to evaluate the material with common AM printing strategies that partially mitigate the underlying anisotropic properties.

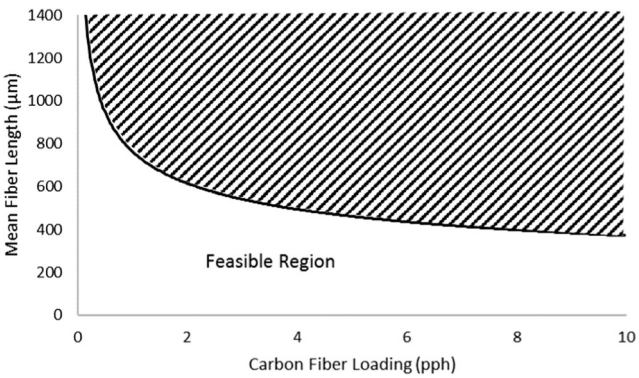

Fig. 1 Feasible ink processing window for the range of inks tested. The boundary is determined by the minimum mixing time to achieve adequate fiber dispersion

Table 1 Test ink composition and mix time

CF loading	Min mix time[a]
0 pph (base ink)	N/A
1 pph (0.6 vol%)	2 min
4 pph (2.3 vol%)	4 min
7 pph (3.9 vol%)	6 min
10 pph (5.5 vol%)	8 min

[a] after addition of carbon fiber tape

Clay content for all inks was held constant at 10 pph, or about 5 vol%, resulting in a rheological yield stress of 168 Pa for base ink. This was qualitatively determined to be the minimum for printing self-supporting structures of sufficient height to create the test specimens. Minimal clay loading has several advantages: Lower viscosity facilitates separation of the chopped fiber tape under high-shear mixing, resulting in shorter mix times. It also reduces the viscosity of the fiber-loaded inks, which keeps extrusion pressures reasonable (less than 0.8 MPa for 10 pph CF ink). Finally, nanoclay itself has been shown to increase epoxy strength [17], but because it is often accompanied by a plasticizing surfactant the reinforcement is maximized only at low loadings [36]. Minimal clay was used both to permit higher carbon fiber loading and to minimize convolution of the reinforcement effects of the carbon fiber and the clay. Using this base ink, the upper limit for carbon fiber loading was found to be 10 pph for the mixing method employed. Beyond this limit, the resulting paste could not fully break up the tape to form an extrudable direct write ink.

Fiber Measurement Methods

To quantify the carbon fiber length variation as a function of mixing time, samples were taken at 1- to 2-min increments from the mixtures. These samples were diluted with epoxy, and the diluted solution was placed on a glass slide and imaged via optical microscopy at 5x magnification. Prior to image analysis, multiple images were stitched together to increase the number of full-length fibers analyzed without losing image resolution, thereby increasing measurement accuracy. On average over 300 fibers were measured for each ink-time combination (Appendix Table 3). Microscopy images were then analyzed using ImageJ Ridge Detection plugin [37], which detects fibers and quantifies lengths from binary images.

Mechanical Testing Methods

3-point bending and uniaxial tensile testing were performed to characterize the properties of the cured inks. At least 5 tensile and flexural samples were fabricated and tested for each ink configuration. Constant cross head speeds of 1 mm/min and

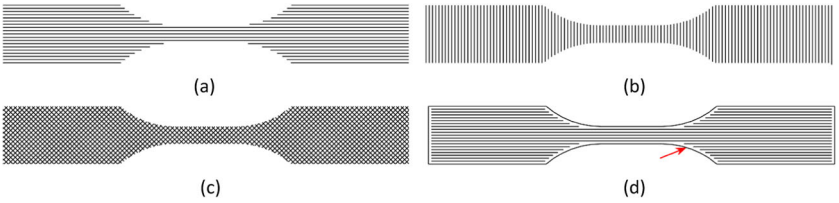

Fig. 2 AM sample raster printing orientations: (**a**) 0°; (**b**) 90°; (**c**) ±45°; (**d**) Example of voids between raster and perimeter roads

6 mm/min were utilized for tensile and 3-point bending tests, respectively. 3-point bending tests followed ASTM D7264 (*Standard Test Method for Flexural Properties of Polymer Matrix Composite Materials*). Specimens were nominally 150 × 12.7 × 3 mm. Actual thickness varied from 2.4 to 3.0 mm, and the support span was adjusted for each sample to achieve a 20:1 span-to-thickness ratio. Flexural strains were calculated using the crosshead displacement according to the ASTM D7264 test standard:

$$\varepsilon = \frac{6\delta h}{L^2} \tag{1}$$

where ε is the flexural strain, δ is the crosshead displacement, h is the beam thickness, and L is the support span length. Flexural stress was obtained using the formula given in the ASTM D7264 standard according to

$$\sigma = \frac{3PL}{2bh^2} \tag{2}$$

where P is the applied force, b is the width of the beam, and h is the thickness of the beam. This equation assumes the breakage of the specimens at midpoint of the support span; however, in the flexural experiments, offset of fracture locations relative to the midpoint was observed for some specimens. For these samples, equation (2) was modified using the correct bending moment at the fracture location. Flexural modulus was calculated as the slope of the flexural stress and strain data per ASTM standard.

Tensile tests followed ASTM D638 (*Standard Test Method for Tensile Properties of Plastics*) and the specimens were fabricated accordingly. Per the standard, gauge length of the tensile samples was 7.62 mm, gauge width was 3.18 mm, and the total length of the tensile coupons was 63.5mm. Tensile stress was determined as the ratio of the tensile force and cross sectional area of the gauge section. Digital image correlation (DIC) was used to measure strain in all tensile test specimens. White paint was sprayed in speckle form on sample surfaces as a contrast enhancer. Successive images were then taken during the mechanical testing and analyzed using VIC-2D 2009 DIC software to obtain strain field under tensile loading. Ultimate tensile strength was measured as the tensile stress achieved at failure, and elastic modulus was calculated as the slope of the tensile stress and strain data per ASTM standard.

Sample Preparation

Both AM and compression molded samples were fabricated from the ink formulations shown in Table 1. The curing temperature profile for all samples was 100 °C for 15 h followed by 220 °C for 2 h. Degree of cure was 100% as estimated by differential scanning calorimetry.

AM samples were fabricated on an nScrypt 3Dn-500 printer. Ink was loaded into 10 cc Nordson dispensing syringes which were centrifuged in a Fisher Scientific Accuspin 400 at 4000 RPM for 20 min to remove entrapped air and then transferred to another syringe as a secondary air-removal step. Ink was pneumatically deposited via a Nordson Ultimus V pressure-controlled dispenser. The most viscous ink (10 pph CF) required the use of a Nordson High-Pressure Tool, which amplified the pump pressure by a factor of 3.3. Ink was extruded through a Nordson tapered nozzle with 580 μm diameter. Target printing parameters were a deposition rate of 3.75×10^{-3} cc/s and a printing speed of 15 mm/s, resulting in nominal road width and layer height of 500 μm. The build plate was borosilicate glass covered with PTFE coated aluminum foil.

AM processes generally produce poor surface finishes, and extrusion-based processes inherently create voids where raster roads terminate at perimeter roads (Fig. 2(d)). This can make it difficult to differentiate failure caused by surface roughness or defects from failure of the material itself. To ensure that the underlying material strength was measured, the top surfaces of

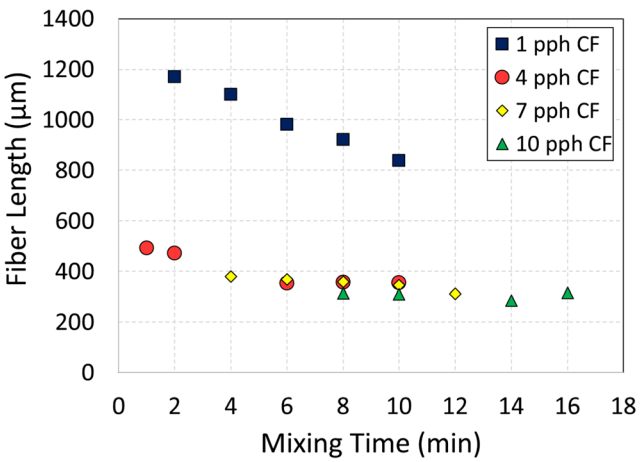

Fig. 3 Effect of mixing time on mean fiber length for inks fiber-loaded inks

Table 2 Mean carbon fiber length (μm) for tested inks

Ink	Sample mean length (μm)	Aspect ratio
1 pph (2 min)	1171	234:1
4 pph (4 min)	413	83:1
7 pph (6 min)	370	74:1
10 pph (8 min)	315	63:1

AM test samples were machined to improve surface finish. This facilitated repeatable thickness measurements, created a well-defined neutral axis for flexure testing, and eliminated stress concentrations that could lead to premature failure in tension. Exceptions were the cross-hatched and quasi-isotropic samples, which were tested with as-printed surfaces to alleviate concern that the layer sequence would be perturbed by partial removal of the outer layer. To prevent voids in radii of the gauge section, the tensile samples were waterjet cut from 77 × 48 mm printed plates. Flexure samples, which are prismatic, were printed directly.

Compression molded samples were prepared from the same inks used to create the AM samples. The inks were spread into 152.4 × 152.4 mm (6 × 6 in) square molds with 3 mm depth and compressed between two steel metal plates under 3000 N force. The full curing cycle (15 h at 100 °C followed by 2 h at 220 °C) was completed under compression. After the square plates were taken out of the mold, tensile and 3-point bending test samples were waterjet cut.

Results & Discussion

Fiber Length Vs. Mix Time

Mean fiber length decreased with both fiber loading and mixing time; however, there is a limit with respect to both parameters (Fig. 3). Results suggest that fiber length is independent of loading above 4 pph (2.3 vol%) and appears to reach a steady state value of about 300 μm regardless of fiber loading and mixing time. Mean fiber lengths for the inks subjected to mechanical testing are shown in Table 2.

Fiber length distributions offer additional insight. All are skewed toward shorter fiber lengths, as exemplified in Fig. 4(a) for 10 pph CF ink mixed for 8 min, and were modeled as Weibull distributions [38]:

$$f(x) = \begin{cases} \frac{\beta}{\alpha^{\beta}} x^{\beta-1} e^{-(x/\alpha)^{\beta}} & x \geq 0 \\ 0 & x < 0 \end{cases} \quad (3)$$

where α and β are the Weibull scale and shape parameters, respectively.

Distribution parameters for all data are presented in Appendix Table 3, and the evolution of the distribution morphology with time for one ink (10 pph CF) is illustrated graphically in Fig. 4(b). As mixing proceeds, the Weibull shape parameter (β) tends to increase, reducing the degree of left skew, and the variance of the distribution tends to decrease. The peak of the distribution, which may roughly be interpreted as the most probable fiber length, shifts toward the apparent steady state mean of 315 μm. By way of comparison, the critical fiber length is calculated to be 305 μm according to [33].

$$l_c = \frac{\sigma_r d\sqrt{3}}{2\sigma_m} \quad (4)$$

where d is the fiber diameter and σ_r and σ_m are the ultimate strengths of the reinforcement and the matrix, respectively. Notably, mixing likely creates very few small fiber fragments that are beyond our techniques ability to accurately measure. For example, even at maximum mix time, more than 98% of fibers in the 10 pph CF ink were recorded as being longer than 100 μm (aspect ratio > 20).

These results indicate that fiber loading and initial length play important roles in the evolution of the fiber length distribution. Higher loadings increase the probability of collision

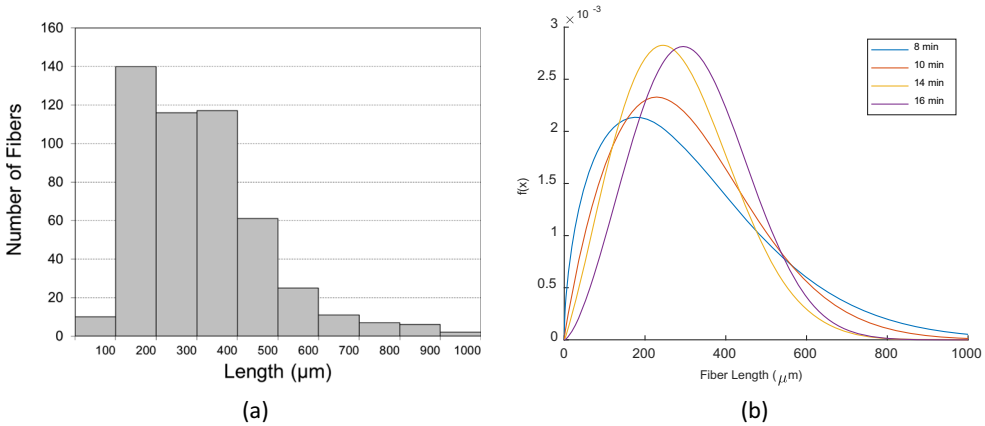

Fig. 4 Fiber length distribution for 10 pph CF ink: (**a**) Histogram for 8-min mix time; (**b**) fitted Weibull distributions for all mixing times examined

between fibers, and longer fibers are more easily fractured. This is evidenced by the rapid decrease in mean length from the initial 6000 μm tape length in the first 1–2 min and by the difference in the 1 pph CF ink versus the higher loadings. As mixing proceeds, the frequency of very short fiber lengths (< 100 μm) is not recorded as having increased significantly, indicating that either shorter fibers are less likely to break further or that the process used has less sensitivity to shorter fibers which are the more difficult to measure fibers. As the fibers at the longer end of the distribution continue to fracture, the variance decreases, and the distribution peak moves right. At the longer mixing times, the change in distribution parameters diminishes and appears to approach a quasi-steady state that resembles a Gaussian distribution. Measurement of the fiber lengths for selected inks before and after printing gave the same average fiber length within 1%, indicating that the printing process did not significantly affect the fiber length distribution.

Mechanical Properties: Longitudinal AM & Compression Molded

Figure 5 shows the mechanical testing results for AM (longitudinal print direction) and compression molded samples. The addition of clay (base ink) significantly increases flexure strength and stiffness, similar to [27], and the results show that this effect extends to tensile strength and stiffness. Strength and stiffness exhibit additional increase as carbon fiber loading is increased. The highest strength and stiffness occur in the AM samples at 10 pph (5.5 vol%) carbon fiber, which represents a 236% increase in tensile strength, 189% increase in flexure strength, 259% increase in Young's modulus, and 232% increase in flexure modulus over neat epoxy.

Regarding the tradeoff between fiber length and loading along the upper boundary, the results indicate that the effect of carbon fiber loading dominates that of fiber length within the range of parameters tested. If an optimal point exists where reduced fiber length offsets higher carbon fiber loading, it is beyond the 10 pph loading point, and exploration of this space will require different ink processing methods.

Figure 5 also indicates that longitudinal AM samples outperformed those made by compression molding. Tensile and flexure strength are 30 and 33% higher, respectively, for the 10 pph CF AM samples. Stiffness is also greater by 47% in tension and 52% in flexure. The most likely explanation is fiber alignment in the printing direction, which can be qualitatively observed via SEM and X-ray CT imaging. Figure 6 shows SEM images of fracture surfaces, where exposed fibers on the AM samples exhibit significantly more uniform directionality. Figure 7(a) and (b) shows CT cross sectional images, revealing significantly more fiber alignment in the AM sample. Figure 7(c) is a 3-D visualization of fibers in an AM sample constructed from CT images, illustrating that most fibers are aligned reasonably well in the print direction.

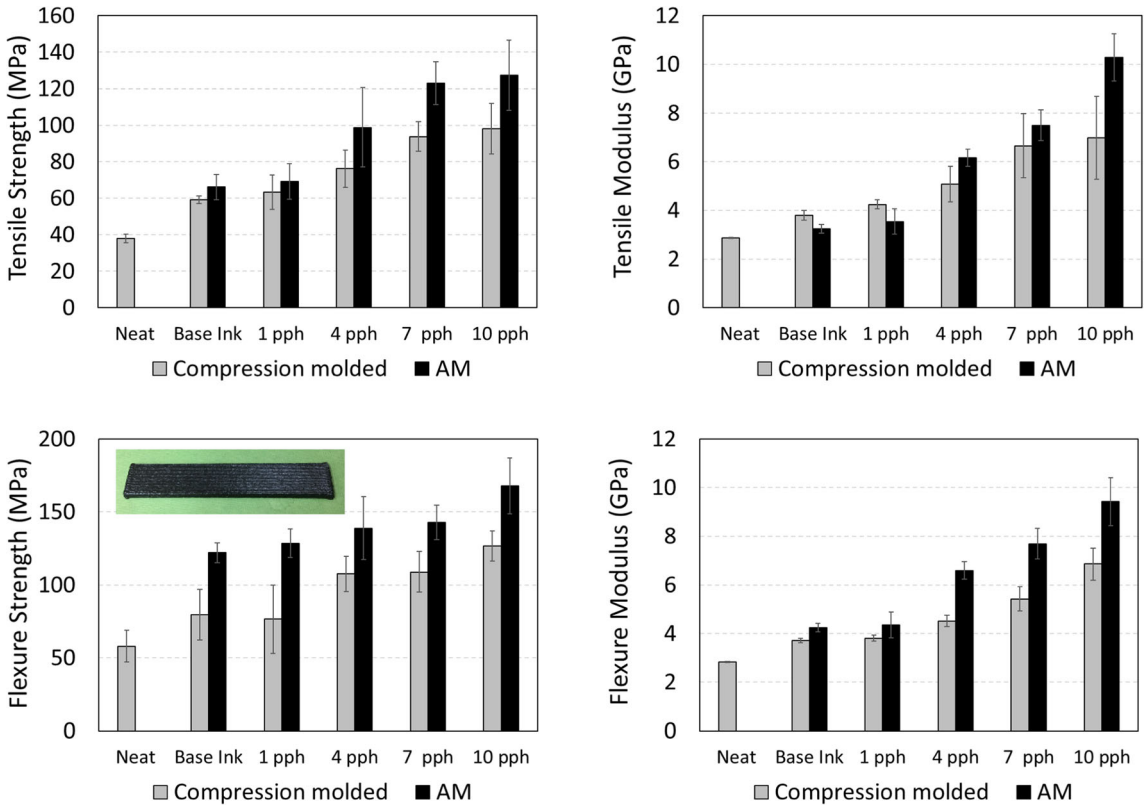

Fig. 5 Mechanical testing results for AM and compression molded samples. Error bars represent the 90% confidence interval for the mean

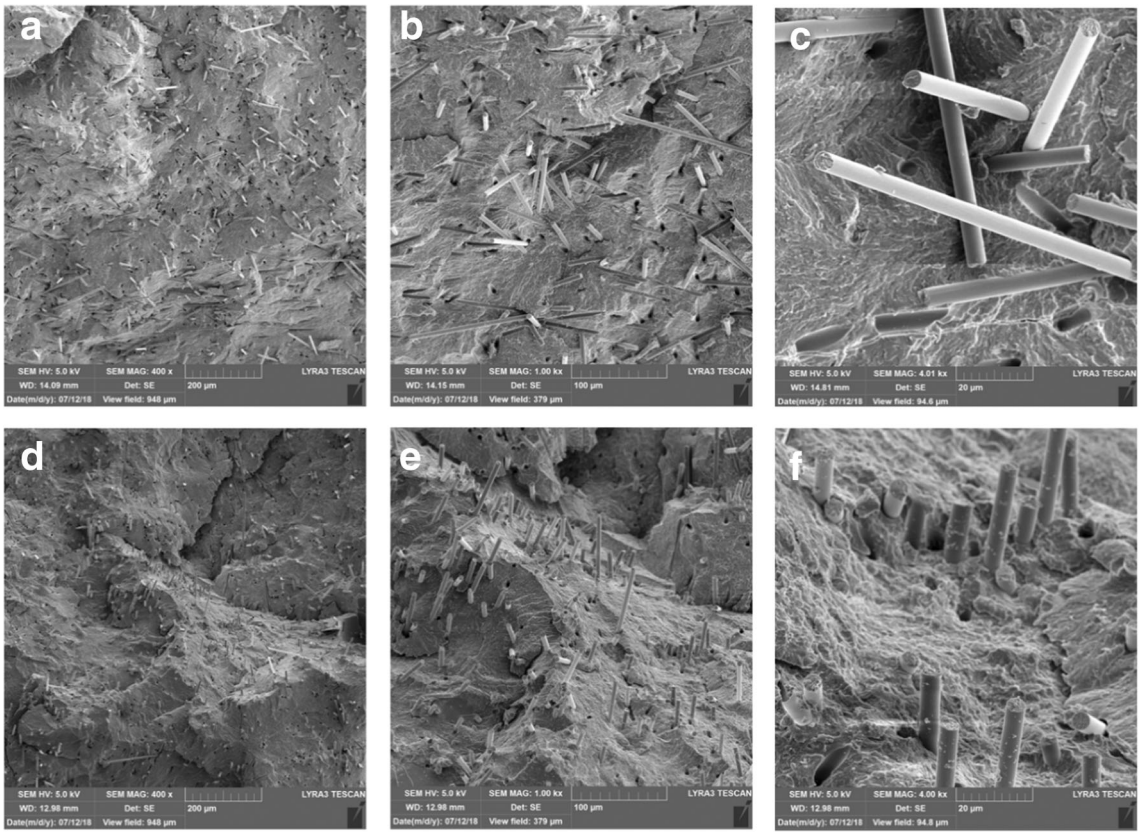

Fig. 6 SEM images of fracture surfaces: Compression molded samples at 400x (**a**), 1000x (**b**), and 4000x (**c**). AM samples at 400x (**d**), 1000x (**e**), and 4000x (**f**)

The quality of alignment was further quantified via calculation of Herman's orientation parameter. Two-dimensional slices were extracted from the x-ray CT volume in Fig. 7(c), as shown in Fig. 8(a). A sample image is shown in Fig. 8(b). ImageJ was used to perform a fast Fourier transform (FFT) for each x-ray CT slice, an example of which is shown in Fig. 8(c). Azimuthal integration was performed in Fit2D about the red circle indicated in Fig. 8(c). The resulting intensity plot is shown in Fig. 8(d) after background subtraction. The ensemble average was calculated as

$$\cos^2\varphi = \frac{\sum_i I_i \sin\varphi_i \cos^2\varphi_i}{\sum_i I_i \sin\varphi_i} \tag{5}$$

Where I_i is the intensity about the azimuth at a given scattering angle and φ_i is the fiber angle with respect to the printing direction. Herman's orientation parameter was calculated as

$$S_d = \frac{3\cos^2\varphi - 1}{2} \tag{6}$$

Analyzing 5 images yielded an average orientation parameter of about 0.6. This result is interpreted on a scale of −0.5 (perpendicular to the print direction) to 0 (random) to 1 (perfectly aligned in the print direction) and indicates good alignment, but with room for improvement.

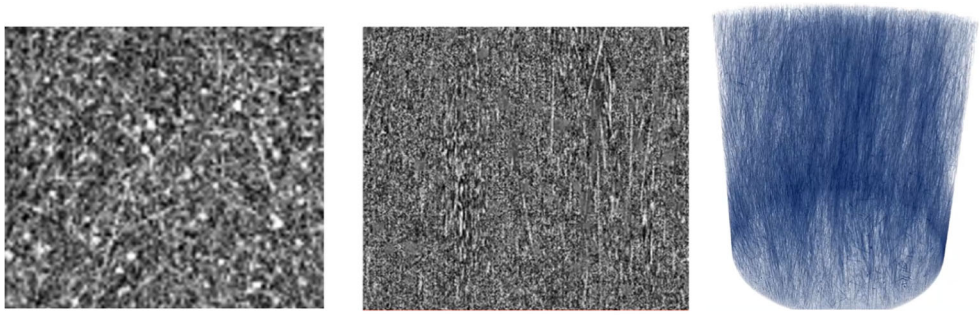

Fig. 7 X-ray CT imaging of test samples: (**a**) compression molded planar image, (**b**) AM planar image, and (**c**) 3D visualization of fibers in an AM sample

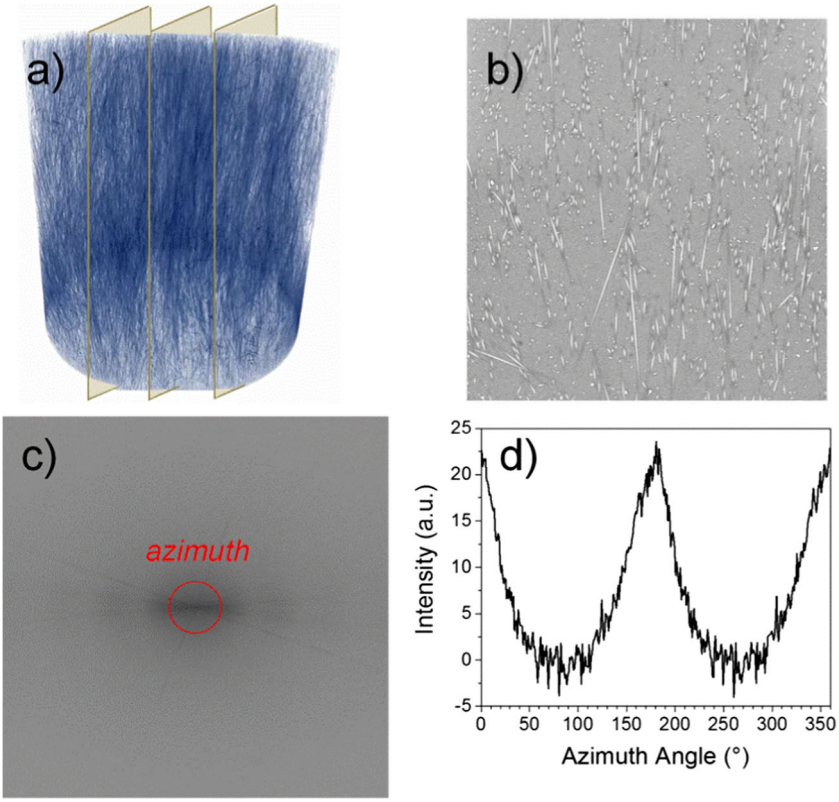

Fig. 8 Fiber orientation parameters in a printed 10 pph CF coupon was measured from the x-ray CT volume (**a**) which was divided into 2D slices (**b**) from which FFTs (**c**) were obtained and orientation parameters were calculated from azimuthal intensity data (**d**)

Comparison of Experimental Results to Analytical Model Predictions

Experimental data are compared to predictions according to the models by [32, 33]. The elastic modulus of a material with aligned fibers is calculated as

$$E_{Aligned} = \frac{(1 + 2s\eta_L f)E_m}{1-\eta_L f};\ \ \eta_L = \frac{(E_r/E_m - 1)}{(E_r/E_m + 2s)} \tag{7}$$

where s is the aspect ratio of the fibers, f is the fiber volume ratio, and E_r and E_m are the elastic moduli of the reinforcement and matrix, respectively. The elastic modulus of a material with randomly oriented fibers is calculated using the modulus in both longitudinal and transverse directions:

$$E_{Random} = \frac{3}{8}E_L + \frac{5}{8}E_T \tag{8}$$

where E_L and E_T are the elastic moduli in longitudinal and transverse directions and obtained by

$$E_L = \frac{(1 + 2s\eta_L f)E_m}{1-\eta_L f};\ \ \eta_L = \frac{(E_r/E_m - 1)}{(E_r/E_m + 2s)} \tag{9}$$

and

$$E_T = \frac{(1 + 2s\eta_T f)E_m}{1-\eta_T f};\ \ \eta_T = \frac{(E_r/E_m - 1)}{(E_r/E_m + 2)} \tag{10}$$

Strength predictions are also made using models described in [32, 33]. It is assumed that the ultimate strength is equal to the yield strength since no yielding was observed prior to failure as shown by the representative stress-strain data in Appendix Figs. 16 and 17. The ultimate strength of a material with aligned fibers is calculated as

$$\sigma_{Aligned} = \begin{cases} fs\frac{\sigma_m}{\sqrt{3}} + (1-f)\sigma_m, & s < s_C \\ f\sigma_r\left(1 - \frac{\sigma_r\sqrt{3}}{4s\sigma_m}\right) + (1-f)\sigma_m, & s \geq s_C \end{cases} \tag{11}$$

where s is the aspect ratio of the fibers, f is the fiber volume ratio, and σ_r and σ_m are the ultimate strengths of the reinforcement and the matrix, respectively. s_C is the critical aspect ratio,

$$s_C = \frac{\sigma_r\sqrt{3}}{2\sigma_m} \tag{12}$$

The strength of a material with randomly oriented fibers is calculated using the directional strengths:

$$\sigma_{Random} = \frac{3}{8}\sigma_L + \frac{5}{8}\sigma_T \tag{13}$$

where σ_L and σ_T are the strength in longitudinal and transverse directions and are obtained by

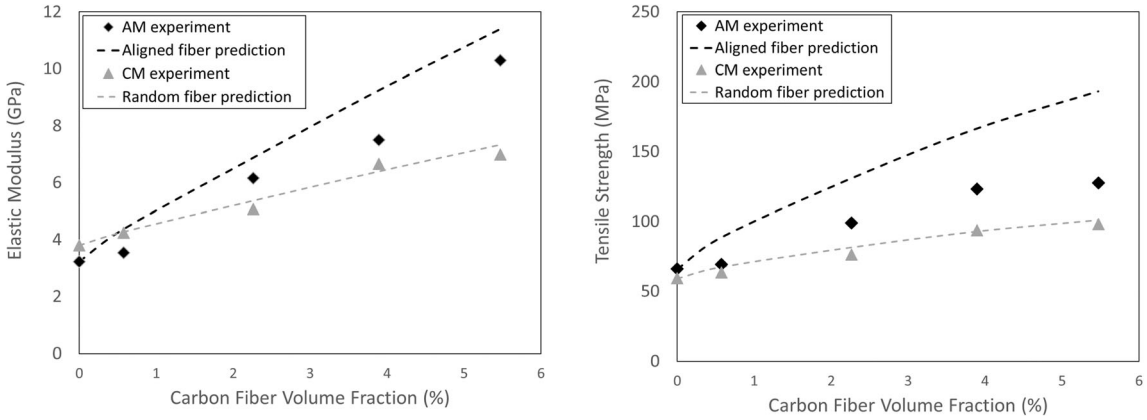

Fig. 9 Experimental data and analytical model comparison of AM and compression molded (CM) composites for (**a**) elastic modulus and (**b**) ultimate tensile stress

$$\sigma_L = \begin{cases} fs\frac{\sigma_m}{\sqrt{3}} + (1-f)\sigma_m, & s < s_C \\ f\sigma_r\left(1-\frac{\sigma_r\sqrt{3}}{4s\sigma_m}\right) + (1-f)\sigma_m, & s \geq s_C \end{cases} \quad (14)$$

and

$$\sigma_T = \sigma_m\left(\frac{f}{\sqrt{3}} - f + 1\right) \quad (15)$$

In implementing these models, tensile properties for base ink from Fig. 5 are used for the matrix properties, E_m and σ_m. Properties of the carbon fiber are reported as $E_r = 4619$ MPa and $\sigma_r = 231$ GPa [39].

Figure 9 shows the experimental results for both longitudinally printed AM and compression molded samples relative to the predicted values for aligned and randomly oriented fibers. The compression molded composite results closely match the random fiber orientation predictions. The general trend of the AM results is similar to the aligned prediction, though magnitudes are marginally lower due to the fact that the models in equations (7–15) assume perfect fiber alignment. If the process could be optimized so as to improve fiber alignment (increase S_d from 0.6 to approximately 0.8–0.9), it is likely that full theoretical strength and stiffness could be achieved.

Equation (12) also yields insight as to why fiber loading dominated fiber length effects along the upper edge of the processing window in Fig. 1. The critical aspect ratio, s_C, for the AM samples was calculated to be 61, corresponding to a length of 305 μm. From equation (14), the effect of maintaining a fiber length above this threshold is small. It is seen in Table 2 that mean fiber length is above this threshold for all inks, indicating that the additional length attained at lower fiber loadings does not compensate for the lower volume fraction of reinforcing material. However, the mean aspect ratio

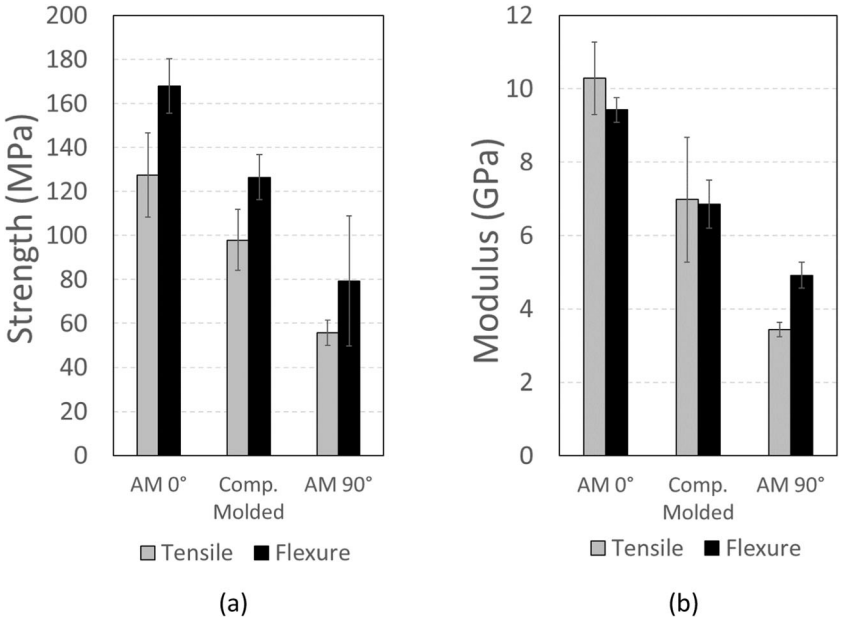

Fig. 10 Comparison of (**a**) 10 pph CF AM samples printed in the transverse (90°) direction vs. compression molded samples, and (**b**) 10 pph CF AM samples printed in the longitudinal (0°) direction. Error bars represent the 90% confidence interval for the mean

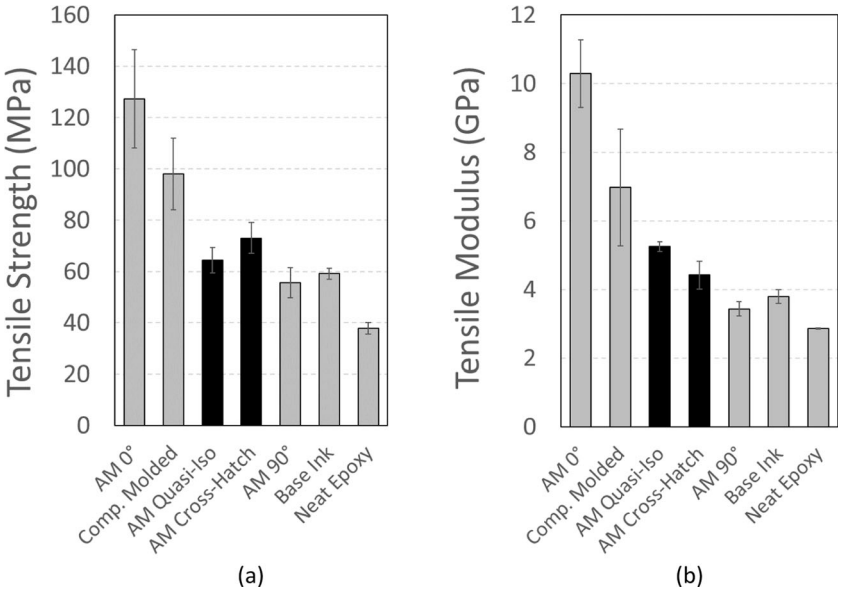

Fig. 11 Comparison of (**a**) tensile properties for quasi-isotropic and (**b**) crosshatch printing patterns. All samples were printed from 1010 ink. Error bars represent the 90% confidence interval for the mean

for 10 pph CF ink (5.5 vol%) is 63 – very close to the calculated threshold. This suggests that the hypothesized tradeoff between length and loading may exist just beyond the range tested. This can be seen in the AM experimental data Fig. 9(b), where the curve appears as if it is reaching a maximum at 5.5 vol%.

Printing Direction

Mechanical testing results for AM samples printed with 10 pph CF ink in the transverse (90°) direction are shown in Fig. 10. Transverse samples are weaker and less stiff than both longitudinally (0°) printed and compression molded samples due to transverse fiber alignment.

Figure 11 includes a comparison between the same transverse samples and base ink printed in the longitudinal direction, indicating no statistically significant difference between the two. The fact that transverse fiber orientation did not decrease the strength of the base material is significant for two reasons. First, stress concentrations at the fiber-matrix interface are a concern in chopped fiber composites because they can outweigh the reinforcement benefits, possibly resulting in lower strength than the unreinforced matrix material. This is of particular concern when fiber orientation is transverse to the load and the reinforcement effect is at its minimum. The results give no indication of this problem. Second, AM processes – most notably thermoplastic extrusion processes – usually exhibit reduced transverse strength because road-to-road bond strength is typically lower than the base material strength. The results indicate that this is not the case for this material, which suggests that this process may not suffer from the same road-to-road bonding issues as FFF.

Since anisotropic properties are a well-known side effect of additive processes, AM parts are frequently printed using a multidirectional layer pattern to mitigate anisotropies in the printing plane. Figure 11 shows tensile results for two of these patterns: quasi-isotropic (bottom to top: 0°, 45°, −45°, 90°, 90°, −45°, 45°, 0°) and crosshatch (45°, −45°). Cross sectional views are provided in Fig. 12. While the crosshatch samples had slightly higher strength versus the quasi-isotropic

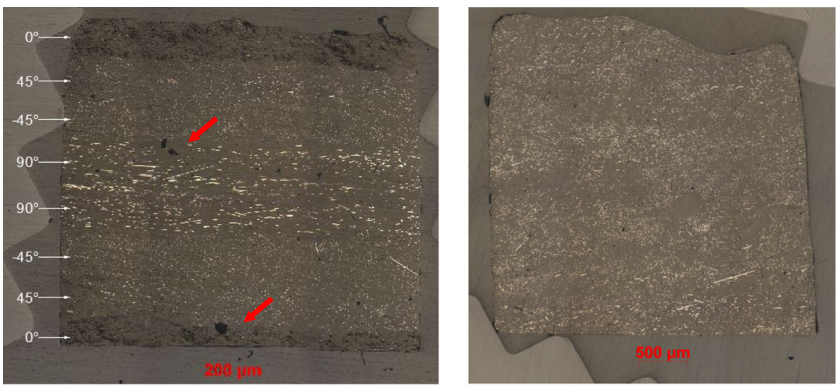

Fig. 12 Optical microscopy of polished cross sections for (**a**) quasi-isotropic and (**b**) crosshatch 10 pph CF samples. Arrows indicate porosity caused by bubbles entrapped in the ink during syringe loading

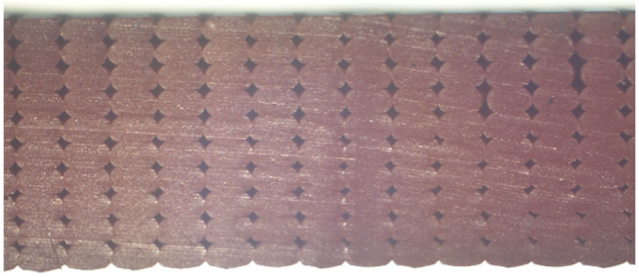

Fig. 13 Cross section of a thermoplastic (ABS) structure showing inter-road porosity typical of the FFF process. Test samples printed for this study do not exhibit such porosity

samples, quasi-isotropic exhibited a slight improvement in stiffness. Both patterns outperformed base ink but were not as strong or stiff as compression molded parts. It is important to note that while these samples were waterjet cut from a printed block, the top surface was not machined (due to concern of disrupting the directional pattern), and thus was not as smooth as the compression molded parts. It is possible that this surface introduced stress concentrations which adversely affected the tensile strength. It is also apparent from Fig. 12(a) that the top and bottom layers – which are the longitudinal layers that should contribute most to strength and stiffness – are thinner compared to the other layers.

Porosity

Figure 12 also illustrates the low level of porosity which may be achieved via direct write thermoset composite printing. This stands in sharp contrast to the porosity typically created by extrusion-based AM processes, especially thermoplastic FFF (Fig. 13). Low porosity is possible due to the pseudoplastic nature of the inks. Extrusion reduces viscosity by 2–3 orders of magnitude for approximately 1 s, allowing newly printed

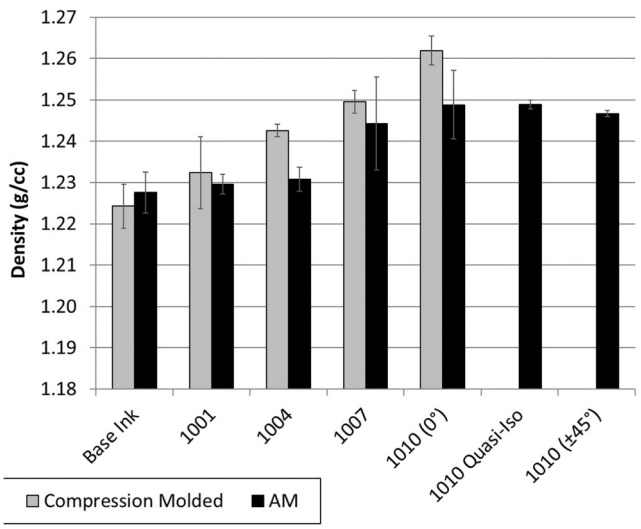

Fig. 14 Density of test samples

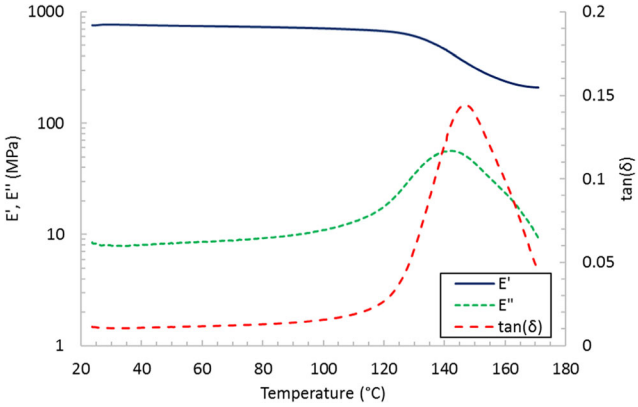

Fig. 15 Representative DMA plot for 10 pph CF material

roads to flow together with the existing structure, resulting in near-full-density parts. Density of the test samples, as measured by the Archimedes method, reveal that AM samples are within 1% of compression molded samples (Fig. 14). Figure 14 also indicates that printing direction does not significantly affect density. What little porosity does exist in AM samples is exemplified in Fig. 12, where entrapped air bubbles in the ink are transferred to the printed part. Air bubbles occur in the manual syringe loading process due to high ink viscosity (on the order of 10^4 to 10^5 Pa-s), and not all are removed by centrifuging.

Glass Transition Temperature

10 pph CF ink samples were subjected to dynamic mechanical analysis (DMA) testing to assess glass transition temperature, T_g, and were found to have an average T_g of 132 °C and match that of the base ink. A representative DMA plot is shown in Fig. 15. By way of comparison, typical T_g values for common thermoplastic FFF materials are 27 °C for Nylon 6, 51.4°C for polylactic acid (PLA) biopolymer, 74 °C for polyethylene terephthalate (PET), and 108 °C for acrylonitrile butadiene styrene (ABS) [40]. This result is an important step in filling the gap in current AM capabilities regarding printing temperature-resistant polymers.

Conclusions

This research demonstrated an AM process for epoxy matrix chopped carbon fiber composites that represents a step toward filling the void in polymer AM process capabilities at the intersection of high specific strength, specific stiffness, temperature, and environmental durability. It has also generated insight into key process-property interactions by 1) investigating the relationship between ink mixing parameters and fiber length distribution, and 2) exploring the influence of manufacturing process, fiber loading, fiber length, and printing direction on mechanical performance. Fiber length distributions were modeled as Weibull distributions. As mixing progressed, these distributions became

Gaussian-like and the mean tended toward a steady state value of roughly 300 μm, which was shown via analytical modeling to exceed the critical aspect ratio for strength. Imaging confirmed good fiber alignment in the print direction, and empirical results agree with theoretical predictions that the AM process yields higher unidirectional strength and stiffness as compared to compression molding. Transverse printing and fiber alignment did not reduce the strength or stiffness of the base material, as is the case in other extrusion-based AM processes, and the density of the AM structures was within 1% of compression molded samples. Quasi-isotropic and crosshatched layer topologies, which are frequently employed in AM to mitigate material anisotropy, showed higher strength and stiffness as compared to unreinforced epoxy, but underperformed compression molding. These results represent an important step forward toward the development of additive manufacturing for high strength- and stiffness-to-weight ratio components operating at elevated service temperatures.

Acknowledgements The authors would like to acknowledge the financial support for the AFRL Summer Faculty Program, Minority Leaders Program, and International Cooperative Research and Development Fund, as well as the technical contributions from Prof. Brett Compton on ink formulation.

Appendix 1

Table 3 Fiber length (μm) distribution parameters

Ink	Mix time (min)	Sample size	Weibull parameters		Mean[a]	Std dev[a]
		n	α	β	$\hat{\mu}$	$\hat{\sigma}$
1 pph CF	2	99	1288	1.35	1182	887
	4	189	1213	1.35	1112	834
	6	223	1102	1.50	995	677
	8	186	1023	1.41	931	667
	10	249	947	1.66	846	523
4 pph CF	1	326	555	1.52	500	335
	2	305	537	1.99	476	250
	6	272	402	2.03	356	184
	8	388	406	2.24	360	170
	10	231	402	1.99	357	187
7 pph CF	4	272	431	2.30	382	176
	6	333	418	2.39	370	165
	8	245	406	2.62	361	148
	10	282	391	2.35	347	157
	12	629	355	2.18	314	152
10 pph CF	8	496	351	1.53	316	210
	10	443	350	1.84	311	175
	14	474	323	2.19	286	138
	16	271	360	2.51	320	136

[a] Estimated population parameters

Appendix 2

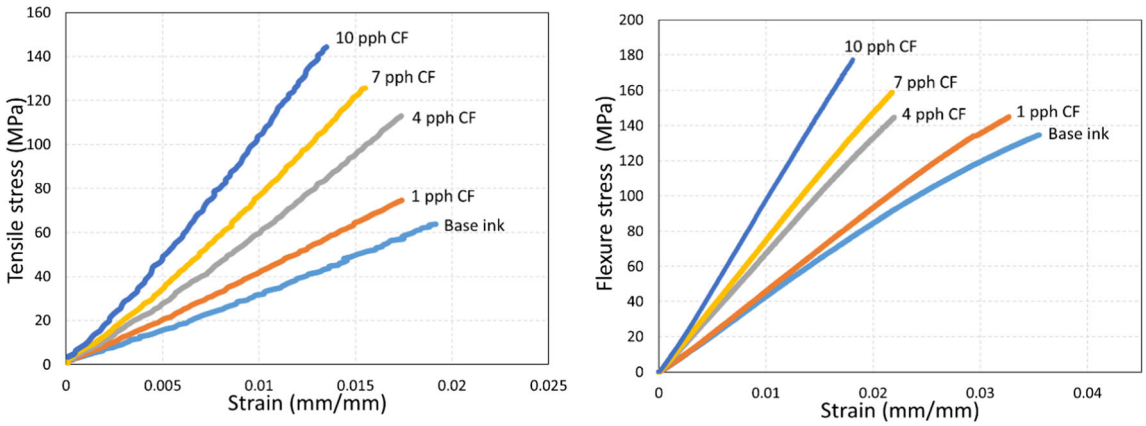

Fig. 16 Representative stress-strain plots for AM samples

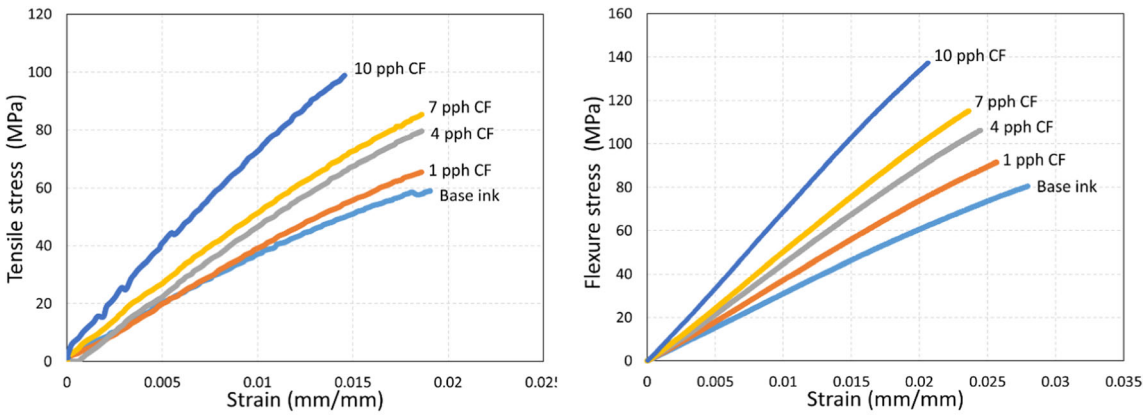

Fig. 17 Representative stress-strain plots for compression molded samples

References

1. Gibson I, Rosen DW, Stucker B (2010) Additive manufacturing technologies. Springer, New York
2. Brackett D, Ashcroft I, Hague R (2011) Topology optimization for additive manufacturing. In: Proceedings of the solid freeform fabrication symposium, Austin, TX
3. Zegard T, Paulino GH (2016) Bridging topology optimization and additive manufacturing. Struct Multidiscip Optim 53(1):175–192. https://doi.org/10.1007/s00158-015-1274-4
4. Yang S, Tang Y, Zhao YF (2015) A new part consolidation method to embrace the design freedom of additive manufacturing. J Manuf Process 20:444–449. https://doi.org/10.1016/j.jmapro.2015.06.024
5. Yang S, Zhao YF (2015) Additive manufacturing-enabled design theory and methodology: a critical review. Int J Adv Manuf Technol 80(1):327–342. https://doi.org/10.1007/s00170-015-6994-5
6. Atzeni E, Salmi A (2012) Economics of additive manufacturing for end-usable metal parts. Int J Adv Manuf Technol 62(9):1147–1155. https://doi.org/10.1007/s00170-011-3878-1
7. Groover MP (2015) Fundamentals of modern manufacturing: materials, processes, and systems, 6th edn. Wiley, New York
8. Mai J, Zhang L, Tao F, Ren L (2016) Customized production based on distributed 3D printing services in cloud manufacturing. Int J Adv Manuf Technol 84(1):71–83. https://doi.org/10.1007/s00170-015-7871-y
9. Kading B, Straub J (2015) Utilizing in-situ resources and 3D printing structures for a manned Mars mission. Acta Astronautica 107:317–326. https://doi.org/10.1016/j.actaastro.2014.11.036
10. Wong JY (2016) 3D printing applications for space missions. Aerosp Med Hum Perform 87(6):580–582. https://doi.org/10.3357/AMHP.4633.2016
11. Cozier AD, Harned KE, Riley MA, Raabe BH, Sommers AD, Pierson HA (2015) Additive manufacturing in the design of an engine air particle separator. Proceedings of the ASME 2015 International Mechanical Engineering Congress & Exposition, Houston, TX. Volume 1: advances in aerospace technology. https://doi.org/10.1115/IMECE2015-51592
12. Boparai KS, Singh R, Singh H (2016) Development of rapid tooling using fused deposition modeling: a review. Rapid Prototyp J 22(2):281–299. https://doi.org/10.1108/RPJ-04-2014-0048
13. Sun Q, Rizvi GM, Bellehumeur CT, Gu P (2008) Effect of processing conditions on the bonding quality of FDM polymer filaments. Rapid Prototyp J 14(2):72–80. https://doi.org/10.1108/13552540810862028
14. Pierson HA, Chivukula B (2018) Process–property relationships for fused filament fabrication on preexisting polymer substrates. J Manuf Sci Eng 140(8):084501–084501-084506. https://doi.org/10.1115/1.4039766
15. Abbott AC, Tandon GP, Bradford RL, Koerner H, Baur JW (2018) Process-structure-property effects on ABS bond strength in fused filament fabrication. Addit Manuf 19:29–38. https://doi.org/10.1016/j.addma.2017.11.002
16. Oztan C, Karkkainen R, Fittipaldi M, Nygren G, Roberson L, Lane M, Celik E (2018) Microstructure and mechanical properties of three dimensional-printed continuous fiber composites. J Compos Mater 53:271–280. https://doi.org/10.1177/0021998318781938
17. Dawoud M, Taha I, Ebeid SJ (2016) Mechanical behaviour of ABS: an experimental study using FDM and injection moulding techniques. J Manuf Process 21:39–45. https://doi.org/10.1016/j.jmapro.2015.11.002
18. Szykiedans K, Credo W, Osinski D (2017) Selected mechanical properties of PETG 3-D prints. Procedia Eng 177:455–461. https://doi.org/10.1016/j.proeng.2017.02.245
19. Letcher T, Waytashek M (2014) Material property testing of 3d-printed specimen in Pla on an entry-level 3d printer. In: Proceedings of the Asme international mechanical engineering congress and exposition, vol 2a
20. Brenken B, Barocio E, Favaloro A, Kunc V, Pipes RB (2018) Fused filament fabrication of fiber-reinforced polymers: a review. Addit Manuf 21:1–16. https://doi.org/10.1016/j.addma.2018.01.002
21. Ning FD, Cong WL, Qiu JJ, Wei JH, Wang SR (2015) Additive manufacturing of carbon fiber reinforced thermoplastic composites using fused deposition modeling. Compos Part B 80:369–378. https://doi.org/10.1016/j.compositesb.2015.06.013
22. Zhong WH, Li F, Zhang ZG, Song LL, Li ZM (2001) Short fiber reinforced composites for fused deposition modeling. Mater Sci Eng A 301(2):125–130. https://doi.org/10.1016/S0921-5093(00)01810-4
23. Quan ZZ, Larimore Z, Wu A, Yu JY, Qin XH, Mirotznik M, Suhr J, Byun JH, Oh Y, Chou TW (2016) Microstructural design and additive manufacturing and characterization of 3D orthogonal short carbon fiber/acrylonitrile-butadiene-styrene preform and composite. Compos Sci Technol 126:139–148. https://doi.org/10.1016/j.compscitech.2016.02.021
24. Araya-Calvo M, López-Gómez I, Chamberlain-Simon N, León-Salazar JL, Guillén-Girón T, Corrales-Cordero JS, Sánchez-Brenes O (2018) Evaluation of compressive and flexural properties of continuous fiber fabrication additive manufacturing technology. Addit Manuf 22:157–164. https://doi.org/10.1016/j.addma.2018.05.007
25. Blok LG, Longana ML, Yu H, Woods BKS (2018) An investigation into 3D printing of fibre reinforced thermoplastic composites. Addit Manuf 22:176–186. https://doi.org/10.1016/j.addma.2018.04.039
26. Compton BG, Lewis JA (2014) 3D-printing of lightweight cellular composites. Adv Mater 26(34):5930–593+. https://doi.org/10.1002/adma.201401804
27. Hmeidat NS, Kemp JW, Compton BG (2018) High-strength epoxy nanocomposites for 3D printing. Compos Sci Technol 160:9–20. https://doi.org/10.1016/j.compscitech.2018.03.008
28. Raney JR, Compton BG, Mueller J, Ober TJ, Shea K, Lewis JA (2018) Rotational 3D printing of damage-tolerant composites with programmable mechanics. Proc Natl Acad Sci U S A 115(6):1198–1203. https://doi.org/10.1073/pnas.1715157115
29. Ozsoy N, Ozsoy M, Mimaroglu A (2016) Mechanical properties of chopped carbon Fiber reinforced epoxy composites. Acta Phys Pol A 130(1):297–299. https://doi.org/10.12693/APhysPolA.130.297
30. Koerner H, Misra D, Tan A, Drummy L, Mirau P, Vaia R (2006) Montmorillonite-thermoset nanocomposites via cryo-compounding. Polymer 47(10):3426–3435. https://doi.org/10.1016/j.polymer.2006.03.057
31. Tandon GP, Weng GJ (1984) The effect of aspect ratio of inclusions on the elastic properties of unidirectionally aligned composites. Polym Compos 5(4):327–333. https://doi.org/10.1002/pc.750050413
32. Ashby MF (2011) Materials selection in mechanical design, 4th edn. Elsevier, Burlington
33. Van Hattum F, Bernardo C (1999) A model to predict the strength of short fiber composites. J Polym Comp 20(4):524–533
34. Ning F, Cong W, Hu Y, Wang H (2017) Additive manufacturing of carbon fiber-reinforced plastic composites using fused deposition modeling: effects of process parameters on tensile properties. J Compos Mater 51(4):451–462. https://doi.org/10.1177/0021998316646169
35. Tekinalp HL, Kunc V, Velez-Garcia GM, Duty CE, Love LJ, Naskar AK, Blue CA, Ozcan S (2014) Highly oriented carbon fiber–polymer composites via additive manufacturing. Compos Sci Technol 105:144–150. https://doi.org/10.1016/j.compscitech.2014.10.009
36. Koerner H, Jacobs J, Tomlin DW, Busbee JD, Vaia R (2004) Tuning polymer nanocomposite morphology: AC electric field

manipulation of epoxy–montmorillonite (clay) suspensions. Adv Mater 16(4):297–302
37. Steger C (1998) An unbiased detector of curvilinear structures. IEEE Trans Pattern Anal Mach Intell 20(2):113–125. https://doi.org/10.1109/34.659930
38. Vardeman SB (1994) Statistics for engineering problem solving. Thomson Learning EMEA, Limited
39. HexCel Corp. (2018) HexTow AS4 carbon Fiber product data sheet. https://www.hexcel.com/user_area/content_media/raw/AS4_HexTow_DataSheet.pdf
40. Zhang SJ, To S (2013) The effects of spindle vibration on surface generation in ultra-precision raster milling. Int J Mach Tools Manuf 71:52–56. https://doi.org/10.1016/j.ijmachtools.2013.04.005